

## Enhancing the Water Capacity in Zr-Based Metal–Organic Framework for Heat Pump and Atmospheric Water Generator Applications

Luna-Triguero, Azahara; Sławek, Andrzej; Huinink, H.P.; Vlugt, Thijs; Poursaeidesfahani, Ali; Vicent-Luna, J.M.; Calero, S.

**DOI**

[10.1021/acsanm.9b00416](https://doi.org/10.1021/acsanm.9b00416)

**Publication date**

2019

**Document Version**

Accepted author manuscript

**Published in**

ACS Applied Nano Materials

**Citation (APA)**

Luna-Triguero, A., Sławek, A., Huinink, H. P., Vlugt, T., Poursaeidesfahani, A., Vicent-Luna, J. M., & Calero, S. (2019). Enhancing the Water Capacity in Zr-Based Metal–Organic Framework for Heat Pump and Atmospheric Water Generator Applications. *ACS Applied Nano Materials*, 2(5), 3050-3059. <https://doi.org/10.1021/acsanm.9b00416>

**Important note**

To cite this publication, please use the final published version (if applicable). Please check the document version above.

**Copyright**

Other than for strictly personal use, it is not permitted to download, forward or distribute the text or part of it, without the consent of the author(s) and/or copyright holder(s), unless the work is under an open content license such as Creative Commons.

**Takedown policy**

Please contact us and provide details if you believe this document breaches copyrights. We will remove access to the work immediately and investigate your claim.

# Enhancing the Water Capacity in Zr-based Metal Organic Framework for Heat Pump and Atmospheric Water Generator Applications

A. Luna-Triguero<sup>a</sup>, A. Sławek<sup>b</sup>, H. P. Huinink<sup>c</sup>, T. J. H. Vlugt<sup>d</sup>, A. Poursaeidesfahani<sup>d</sup>, J.M. Vicent-Luna<sup>a\*</sup>, and S. Calero<sup>a,c\*</sup>

<sup>a</sup>Department of Physical, Chemical and Natural Systems, Universidad Pablo de Olavide, Ctra. Utrera Km. 1, Seville ES-41013, Spain

<sup>b</sup> Faculty of Chemistry, Jagiellonian University, Gronostajowa 2, 30-387 Kraków, Poland

<sup>c</sup> Department of Applied Physics, Eindhoven University of Technology, P.O. Box 513, 5600 MB Eindhoven, The Netherlands.

<sup>d</sup> Engineering Thermodynamics, Process & Energy Department, Faculty of Mechanical, Maritime and Materials Engineering, Delft University of Technology, Leeghwaterstraat 39, 2628CB Delft, The Netherlands

Corresponding authors:

Email: [jmviiclun@upo.es](mailto:jmviiclun@upo.es)

Email: [scalero@upo.es](mailto:scalero@upo.es)

## ABSTRACT

According to the European Commission, in 2016 the residential sector represented 25.4% of the final energy consumption. Heating and cooling in EU households account for 69.1 % of the total energy consumption. The fraction of 84% for heating and cooling is still generated from fossil fuels, and only 16% is generated from renewable energy. To decrease carbon dioxide emissions of fossil fuel consumption, it is crucial to find alternatives to supply the heating and cooling demand. Alternatives such as adsorption-based heat pumps and desiccant cooling systems are receiving much attention because of their moderate energy consumption. These systems are based on reversible exothermic adsorption and endothermic desorption of working fluids. In this work, we combined experiments and simulations to evaluate the viability of several zeolites and MOFs with water for cooling systems applications. We combined the study of adsorption mechanisms and the dynamics of water inside the pores of the structures, thereby obtaining an overall understanding of the working-pair. We found that the Al content in FAU-topology zeolites is a key factor for an efficient process. We also identify ZJNU-30 metal-organic framework as a suitable candidate for cooling applications because of its outstanding water capacity, cooling capacity and coefficient of performance.

## INTRODUCTION

One third of the world energy consumption is generated by households, which is principally used for heating and cooling of residential areas.<sup>1</sup> The energy demand for heating is expected to rise, resulting in a high impact for the global climate change. With the aim of decreasing carbon dioxide emissions of fossil fuel consumption, it is crucial to find alternatives to supply the heating and cooling demand. Adsorption-based heat pumps (AHP) and desiccant cooling systems (DCS) are receiving a great deal of attention due to their moderate consumption of electric power.<sup>2</sup> The working principle of both AHP and DCS systems is governed by reversible exothermic adsorption and endothermic desorption of working fluids in porous materials. In this context, the capacity of the adsorbent must be maximized, and the selected working fluid should have a high enthalpy of evaporation. Commonly used working fluids for these systems are water, methanol, ethanol, and ammonia.<sup>3-7</sup> In this work, we focus on the study of water as working fluid. We select this fluid because in addition of having a high enthalpy of evaporation is the green solvent *par excellence*.

The schematic working mechanism of AHP and DCS is shown in Figure 1a. An initially dry adsorbent is connected to the working fluid (water) evaporator (Fig 1a). During this process, heat is taken from the surroundings by the evaporation of water ( $Q_{ev}$ ). The water is adsorbed inside the pores of the adsorbent. Adsorption is an exothermic process. Therefore, heat ( $Q_{ads}$ ) will be released to the surroundings with at intermediate temperature. As the adsorbent will become saturated with water, regeneration is required (Figure 1b). Energy is taken up at a relatively high temperature ( $Q_{des}$ ) to desorb the water. Next, water is condensed, releasing heat at an intermediate temperature ( $Q_{con}$ ). One can operate this adsorption cycle as a heat pump to generate heat ( $Q_{con}$  and  $Q_{ads}$ ) at an intermediate temperature (AHP) or to generate cold ( $Q_{ev}$ ) at a low temperature (DCS).<sup>8</sup> From an energetic point of view, it would be desirable to have an adsorption isotherm of water with a single and pronounced step. This allows higher thermodynamic efficiency.<sup>9</sup> For realistic applications the step in adsorption should be at  $p/p_0$  between 0.2 and 0.4 (620-1240 Pa), where  $p_0$  represents the saturation pressure of water at room temperature (3100 Pa).<sup>9, 10</sup> The cycle of the AHP consists of four steps (Figure 1b). (1-2) Isosteric heating; the adsorbent is heated from  $T_1$  to  $T_2$  increasing the pressure from  $P_{ev}$  to  $P_{con}$ . The adsorbent is saturated ( $W_{max}$ ) and needs regeneration (desorption); (2-3) Isobaric desorption; adsorbent heating allows water desorption up  $T_{des}$ . When desorbed water ( $W_{max} - W_{min}$ ) is condensed, heat is expelled to the environment in the condenser ( $Q_{con}$ , Figure 1a); (3-4) Isosteric cooling; the system is cooled from  $T_{des}$  to  $T_3$  to reduce the pressure from  $P_{con}$  to  $P_{ev}$ . The adsorbent is regenerated and can be used for adsorption; (4-1) Isobaric adsorption; the cooling continues as the adsorbent retains water. The process finishes at  $T_1$  and the loading is, again, maximal ( $W_{max}$ ). Water has taken up energy from the environment at low temperature in the evaporator ( $Q_{ev}$ ).  $Q_{des}$  is the energy needed for the isosteric heating and the isobaric desorption and  $Q_{ads}$  is the energy expelled during isosteric cooling and isobaric adsorption. For a given working pair, the operational conditions are fixed when  $T_{ev}$ ,  $T_{con}$ , and  $T_{des}$  are chosen. This cycle could be used for heating or cooling, as indicated in Figure 1c. For heating, energy at high temperature ( $T_{des}$ ) is transferred to an intermediate temperature ( $T_{con}$ ,  $T_{ads}$ ). The energy taken from the environment ( $T_{ev}$ ) is also expelled at the intermediate temperature. For cooling systems, it is desirable that the energy taken by evaporation occurs at low temperature ( $T_{ev}$  is subambient temperature). The energy at  $T_{des}$  is used as input energy to generate the cooling effect and  $T_{con}$  or  $T_{ads}$  is rejected. More detailed information on this cycle can be found in literature.<sup>11</sup>

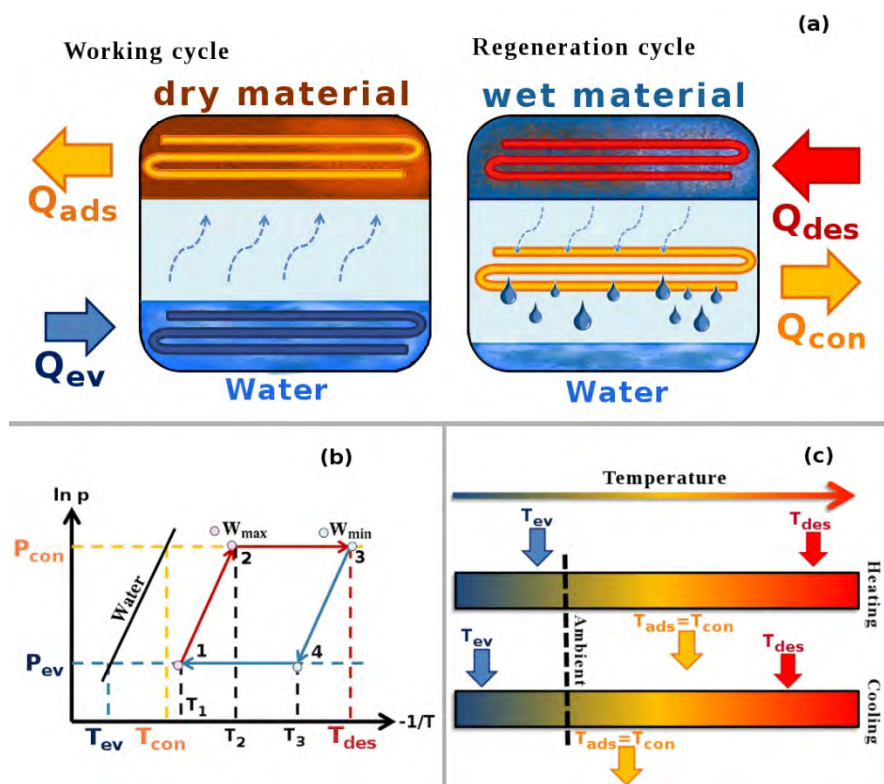


**Figure 1.** (a) Principle of operation of an AHP, adsorption phase (left) and desorption phase (right). Where arrows show the flow of the energy in different stages of the process: heat taken from the evaporator ( $Q_{ev}$ ), heat released at intermediate temperatures ( $Q_{ads}$ ), required energy for desorption ( $Q_{des}$ ), and heat released by the condensed fluid at intermediate temperature ( $Q_{con}$ ). (b) Diagram of the isosteric cycle of an AHP including the vapor pressure of water (black line), temperature and pressure of the evaporator ( $T_{ev}$ ,  $P_{ev}$ ) and the condenser ( $T_{con}$ ,  $P_{con}$ ), desorption temperature ( $T_{des}$ ) and intermediate cycle temperatures ( $T_{1-3}$ ). (c) Modes of operation of a heat pump cycle. Heating (up), cooling (down), ambient temperature (dashed line). Arrows indicate the energy flow taken the heat pump cycle as reference, from low (blue) to high (red) temperature of the thermodynamic process.

Nanoporous materials such as zeolites and metal organic frameworks (MOFs) have been recently reported as candidates for energy storage applications.<sup>2, 12-15</sup> Zeolites are a well-known class of nanoporous crystalline structures based on tetrahedral coordinated T atoms, where T is usually silica or aluminum, linked together by oxygen atoms. Aluminosilicates are negatively charged frameworks compensated by cations. Water adsorption in zeolites could be controlled by varying the framework composition (Si/Al ratio).<sup>16</sup> It is reported that zeolite Y has a sharp step at low  $p/p_0$  due to the high aluminum content. The charge compensation with cations results in a strong hydrophilic character. This strong interaction is useful for gas drying but it becomes a disadvantage for AHP because high temperatures are needed for regeneration. In contrast to zeolite Y, pure silica zeolites have been found to be too hydrophobic materials and the adsorption of water is almost negligible at room conditions.<sup>9, 17</sup>

MOFs are crystalline porous materials constructed by organic ligands connected through metallic clusters.<sup>18</sup> The combination of compositions and topologies result in a virtually infinite number of

possible of structures.<sup>19</sup> Some properties of MOFs such as high porosity, low density, high surface area, and thermal stability make these materials good candidates for applications in gas separation, storage, and catalysis.<sup>20-24</sup> Despite their extraordinary features, another required property is the stability in water.<sup>25</sup> Advances in the synthesis of MOFs have led to water-stable MOFs for adsorption-related applications.<sup>26-30</sup> Numerous zirconium-based MOFs attract attention for their chemical and thermal stability and also for exhibiting stability in water.<sup>31-33</sup> The choice of the adsorbent for water as working fluid is crucial since the hydrophobicity of the material must ensure water nucleation at about 30% of relative humidity (RH).<sup>8,11</sup>

Reversible adsorption or irreversible capillary condensation depends on the pore size of the adsorbent. Below critical pore diameter,  $D_c$ , adsorption is attributed to the cluster formation of the fluid. For pore diameters larger than  $D_c$ , adsorption is due to both capillary condensation and cluster formation. To ensure continuous reversible adsorption and to avoid hysteresis upon water desorption, the pore size of the adsorbent must be lower than  $D_c$ . The critical pore diameter can be expressed as a function of the vapor phase properties of the working fluid as,<sup>34-36</sup>  $D_c = 4\sigma T_c / (T_c - T)$ , where  $\sigma$  is the size of the molecule,  $T_c$  is the critical temperature of the working fluid, and  $T$  is the adsorption temperature. For water ( $\sigma = 2.8 \text{ \AA}$ ), the  $D_c$  is approximately 21  $\text{\AA}$  at room temperature.<sup>34</sup>

In the past years, the capture of fresh water is also receiving attention. The need of clean water is a current reality in deserted climates or in places where water is scarce or contaminated.<sup>37</sup> The use of porous materials to capture and release water is becoming an important research topic. It is a global challenge to ensure the accessibility of fresh water, as this is a fundamental humanity right established by UN in 2010.<sup>38</sup> This can be done by using the changes in the ambient conditions i.e. large temperature and relative humidity differences between day and night.<sup>25, 39, 40</sup> In their current form, atmospheric water generators (AWGs) require high energy and capital costs.<sup>41, 42</sup> Adsorbents with high capacity, steep uptakes at low relative pressures (about 30% of RH at 298 K), and stability upon water treatment/adsorption are promising candidates for friendly environmental AWW applications.<sup>25, 30</sup>

In this work, we combine experimental measurements and molecular simulation to study the viability of selected zeolites and MOFs for adsorption heat pumps (AHP), desiccant cooling systems (DCS), and their operating working windows. To this aim, we studied the molecular mechanisms involved on the adsorption of water in FAU topology zeolites with different composition (high silica and Si/Al=1.06), and in two MOFs based on zirconium metallic center: MOF-841 formulated as  $Zr_6O_4(OH)_4(MTB)_2(HCOO)_4(H_2O)_4$ , and ZJNU-30 MOF formulated as  $[Zr_9O_6(OH)_6(PhCOO)_6(L)_4]24DMA$ .<sup>25, 43</sup> The selected zeolites are commercial adsorbents, they are currently used in scale-up applications. With their reported water stability, and relatively high water capacity, zeolites can be good candidates for AHP and DCS applications. We study here the influence of the composition to choose better working conditions which guarantee an efficient process. On the other hand, Zr-based MOFs are reported to be stable in water, specifically MOF-841 was already proposed for heat pump applications.<sup>25</sup> Our aim here is to compare it with ZJNU-30, a recently synthesized Zr-based MOF with high pore volume and surface area. The selected structures have also a characteristic in common; the size of at least one of the pore of the structures is between 7-10  $\text{\AA}$ . That allows us to study the influence of the pore size of the adsorbents for water

capacity and heat pump applications. The promising properties and the suitable behavior found for the studied structures encourage us to study their transferability to AWG applications. We focus on adsorption mechanisms and thermodynamic properties of the systems, and on the dynamics of water within the pores. There are only a few studies in literature that address the thermal transport and they are focused on water-unstable MOF-5. There is also recent study of Al fumarate.<sup>44-48</sup> We found that controlling the hydrophobicity of the zeolites, i.e. Al content, makes possible their use in realistic AHP and DCS applications, improving the operational windows by decreasing the required temperature for the water desorption. We identify ZJNU-30 as a great candidate for heating and cooling applications with an enormous water capacity and coefficient of performance of 0.948, the best efficiency found up to date. The fast diffusion and transport properties found here ensure that the characteristic cycle times will be suitable for AHP, DCS, and also AWG applications.

## METHODS AND MODELS

### Computational section

Adsorption isotherms and isobars were calculated using Monte Carlo simulations in the grand-canonical ensemble (GCMC), where the chemical potential, volume and temperature are fixed.<sup>49</sup> We used a three step equilibration procedure; first we performed  $5 \times 10^5$  production cycles after  $10^4$  cycles of initialization. Due to the need of water nucleation within the pores, we used the last configuration of molecules as input to perform  $2 \times 10^6$  production cycles. To ensure equilibrium, we repeated this procedure until the average water adsorption converges to the instant adsorption values (see Figure S1). The Ewald summation with a relative precision of  $10^{-6}$  was used to compute electrostatic interactions. The structures are modeled as rigid crystals with the framework atoms placed at the crystallographic positions. We used SPC-E water model.<sup>50</sup> All geometrical and force-field parameters are provided in the Supporting Information (Figure S2). We used generic force-field parameters given in DREADING<sup>51</sup> and UFF<sup>52</sup> for the framework atoms and the metal atoms, respectively. The standard Lorentz-Berthelot mixing rules were used for cross-interaction parameters between MOFs and water molecules. For aluminosilicates, the host-guest and extra-framework cation-guest interactions are parameterized to reproduce the experimental adsorption isobars measured in this work and the adsorption isotherms taken from literature.<sup>25, 53</sup> We used aluminosilicates with FAU topology, NaX (Si/Al  $\approx$  1.06) and high silica FAU (Si/Al  $\approx$  100). Si atoms are distributed randomly over the T-atoms following the Lowenstein rules. Extra-framework cations are placed at the crystallographic positions and are allowed to move during the simulations. The FAU structures were minimized using Baker's method.<sup>54</sup> The simulations were performed in the NPT ensemble using a full-flexible core shell potential to obtain the most energetically favorable structure.<sup>55, 56</sup> The force field parameters, charges, and the cross interaction parameters used for zeolites are listed in Table S1. All the simulations were conducted using the RASPA code.<sup>57-59</sup> The charges for MOFs were calculated using the EQeq<sup>60</sup> method based on Ewald sums.

The amount of molecules adsorbed in porous materials ( $q$ ) is a function of temperature ( $T$ ) and pressure ( $p$ ). The adsorption equilibrium can be described as a plane in the  $p$ - $T$ - $q$  space, ( $F(p, T, q) = 0$ ). The Dubinin-Polanyi theory reduces the two-dimensional description to a characteristic curve  $W(A)$  that expresses the relationship between the adsorption potential  $A$  and the adsorbed specific volume  $W$ .<sup>61, 62</sup> The adsorption potential is the molar Gibbs free energy of adsorption (opposite sign) defined as,

$$A = RT \left( \ln \frac{p_0(T)}{p} \right) \quad (\text{eq 1})$$

where  $p_0$  is the temperature-dependent vapor pressure of water. The amount of water adsorbed expressed as the volume occupied by the adsorbate phase can be approximated by using the liquid phase density:

$$W = \frac{q(p,T)}{\rho_{liq}^W(T)} \quad (\text{eq 2})$$

where  $q$  is the mass adsorbed,  $W$  the volume liquid adsorbed, and  $\rho_{liq}^W$  the liquid density.

To obtain diffusion properties of water inside the cavities of the structures, we performed MD simulations in the NVT ensemble using the GROMACS software.<sup>63-66</sup> The loading of water correspond to that in saturation for each structure. We run  $5 \cdot 10^7$  MD steps with a time step of 1 fs leading to a total simulation time of 50 ns. The trajectory was recorded every 1 ps and the temperature was controlled using the Nose-Hoover thermostat.<sup>67, 68</sup> We calculated the self-diffusion coefficients ( $D_s$ ) of water from the slope of the mean squared displacement using the Einstein equation in the 1-40 ns time interval. The diffusion of water is related to the temperature by the Arrhenius law:

$$D_s = D_0 e^{E_A/k_B T} \quad (\text{eq 3})$$

where  $D_s$  are the self-diffusion coefficients,  $D_0$  is a constant,  $E_A$  is the activation energy of the process,  $k_B$  is the Boltzmann constant and  $T$  is the temperature in K. Activation energies ( $E_A$ ) are calculated from the slope of the natural logarithm of the self-diffusion coefficients as a function of the inverse of the temperature.

## Experimental section

Adsorption isobars of water on NaX and high silica faujasite (HS-FAU) were determined with the use of quasi-equilibrated temperature programmed desorption and adsorption (QE-TPDA) experimental technique. The QE-TPDA measurements were performed with a homemade apparatus, which is a modified flow setup for temperature programmed desorption equipped with a chromatographic TCD detector (Micro Volume TCD, Valco). This setup is described in detail in earlier works.<sup>69, 70</sup>

For the faujasite samples, we used commercial dealuminated HY (Si/Al > 100, Degussa) and NaX (Si/Al  $\approx$  1.06) synthesized in the Fritz Haber Institute in Berlin.<sup>71</sup> HY zeolite was exchanged for Na<sup>+</sup> cations by placing 0.5 g of the sample in contact with 20 mL of 0.5 M NaNO<sub>3</sub> for 3 hours on magnetic stirrer, decanting the mixture and replacing the solution every one hour.

Structures of the studied materials were confirmed by analysis of XRD patterns, which were recorded by a Rigaku MiniFlex powder diffractometer with Cu K $\alpha$  radiation at 10 mA and 10 kV, 2 $\theta$  step scans of 0.02°, and a counting time of 1 s per step. In Figure S3, one can observe a very good agreement between the XRD patterns measured for the samples used for adsorption measurements and patterns modelled from .cif files exploited in molecular simulations. It is important to note that that all peaks for NaX are shifted to left comparing to HS-FAU, which is

consistent with expanding of the periods of the structure from 24.2446 Å (HS-FAU) to 24.9274 Å (NaX).

Prior to adsorption measurements, the studied zeolites were pressed into pellets, crushed and sieved (fraction of 400–500  $\mu\text{m}$  was used). The samples of 7–10 mg were activated before each experiment by heating up to 400 °C (HS-FAU) or 500 °C (NaX) in a flow (6.75  $\text{cm}^3/\text{min}$ ) of pure He (Air Products, purity 5.0). After activation, the flow of carrier gas was switched to helium containing water steam saturated at ambient temperature. After isothermal adsorption was completed, the actual QE-TPDA measurements were performed by heating and cooling samples in a flow of helium containing water steam saturated at RT.

In Figure S4, we presented the QE-TPDA profiles of water on HS-FAU and NaX, which are direct representation of the data measured in the experiments. These profiles consist of desorption maxima and adsorption minima, where their intensities are proportional to the amount of water being adsorbed/desorbed at specific value of temperature. The profiles reveal differences in adsorption of water in the two faujasites. For HS-FAU we observe sharp maxima at relatively low temperature (300–350 K) showing that desorption is sudden, one-stage process taking place in narrow range of temperature, which is of great importance in potential applications for AHP. The hysteresis between desorption and adsorption branches may be caused either by different desorption and adsorption mechanisms, or by deviations of the system from quasi equilibrium conditions.

In sharp contrast to HS-FAU and NaX, the QE-TPDA profiles for NaX are hysteresis free. Desorption maxima and adsorption minima are smoother and are extended over wider range of temperatures (300–675 K). Adsorption at 300–375 K is mostly driven by guest-guest interactions and – due to the conditions of the experiment close to the saturation – can be disturbed by surface-related effects. Most of the water molecules are desorbing/adsorbing at 375–475 K, which is associated to the strongest overall interactions, including guest–host, guest–cations, and guest–guest. At temperature above 475 K, a long tail is seen in the profiles, mainly due to the interactions of the water molecules with cations. These interactions most strongly retain water in NaX zeolite, hindering complete desorption of water from this material, which is significant for the studied applications.

Integration of the QE-TPDA profiles, followed by averaging of the resulting integral profiles, leads to adsorption isobars. More details concerning QE-TPDA methodology and formalism of data reduction can be found in previous work.<sup>72, 73</sup>

The experimental adsorption isobars were also converted to characteristic curves according to above-described methodology.

## RESULTS

Figure 2 shows the Pore Size Distribution (PSD) of the topologies studied in this work. The FAU topology has two types of cavities: sodalite units (ca. 5.5 Å) and large cages (ca. 10.5 Å). MOF-841 consist of cages of ca. 9 Å and interconnected ca. 4.5 Å windows. ZJNU-30 has three types of cages, small cages of ca. 7 Å, intermediate size cages (ca. 14 Å), and large cages (ca. 21 Å). The

size of the cavities was calculated taken into account the Van der Waals radii of the framework atoms. The colors of the spheres represent the pore cages, the studied structures have at least one similar size cavity which is represented in green (from 7 to 11 Å). The adsorption mechanisms strongly depend on the nature and composition of the structures and the size of the cavities in which adsorption takes place.

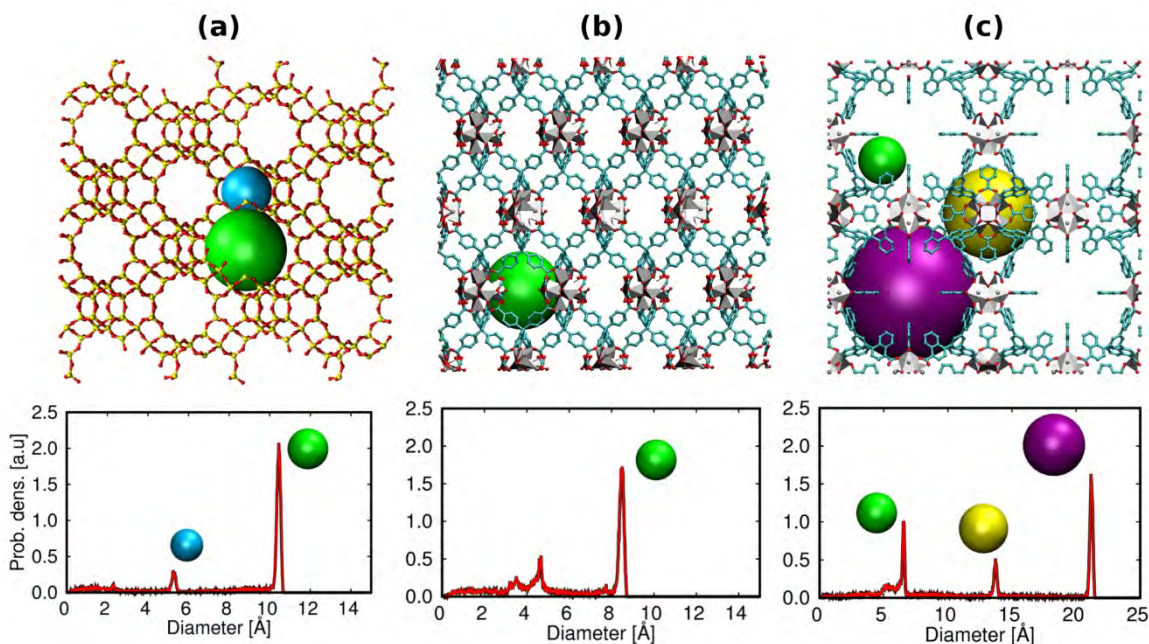


**Figure 2.** Schematic representation of the framework connectivity (top) and pore size distribution (bottom) of (a) FAU zeolite (b) MOF-841, and (c) ZJNU-30. Oxygen atoms in red, T atoms in yellow (Si and Al), carbon atoms in turquoise, Zr metal centers are shown as gray polyhedral and hydrogen atoms are omitted for clarity. The blue, green, yellow, and purple spheres represent the pore cages.

Figure 3 shows the calculated adsorption isotherms of water in NaX (Si/Al=1.06), MOF-841, and ZJNU-30. Comparisons with the experimental data for NaX and for MOF-841 are included in Figure S5. The adsorption in NaX zeolite shows a step at low values of the pressure with a capacity about 320 mg/g. The step of water adsorption in MOF-841 and ZJNU-30 is at approximately  $p/p_0=0.18$  and  $p/p_0=0.22$  (equivalent to RH of about 20%), respectively. We found that ZJNU-30 shows an exceptional sorption capacity for water of about 1200 mg/g.

To have better perspective of the large adsorption capacity of ZJNU-30, it was compared to a very large number of porous structures compiled by de Lange and coworkers.<sup>11</sup> Figure 4 shows the water capacity as a function of the pore volume. The color map indicates the relative pressure (comparable to RH) at which the uptake rises to saturation. Blue color indicates that the step for water adsorption is at low  $p/p_0$  ( $<0.1$ ) at room temperature. These systems need high temperatures for regeneration ( $T_{des}$ ) and therefore are not efficient for AHP such as NaX zeolite (see the isobar of Figure S6). The red-orange indicates water adsorption near saturation pressure ( $p/p_0=0.7-1$ ). These

systems are too hydrophobic and/or show high pore sizes, which cause (1) cryogenic conditions ( $T_{ev} < 273$  K) in the isobaric adsorption (last step of the AHP cycle Figure 1b) and/or (2) hysteresis during desorption, (Cr)-MIL-101 is an example.<sup>74, 75</sup> The desirable relative pressure range is from 0.2 to 0.5 (green) where the structure guarantees enough hydrophobicity. An excellent example is a recent synthesized CoCl(BTDD) MOF with open metal sites (hydrophilic), with pore diameter near to the critical conditions for water (approx. 22 Å), and high capacity (1000 mg/g).<sup>76</sup> On the basis of these results, we proposed ZJNU-30 as excellent candidate for the targeted applications. To the best of our knowledge, ZJNU-30 is a thermal, hydric, and chemically stable Zr-based MOF with the highest sorption capacity for water reported until now (1200 mg/g) at operational conditions. The adsorption starts in the small pores of the structure which are totally interconnected to the medium-size cages and the large pores that allow nucleation at optimal conditions ( $p/p_0=0.2$ ). Moreover, the large cavity has a diameter of 21 Å (Figure 2c) which maximizes the pore volume avoiding irreversible capillary condensation.

As we previously mentioned, NaX zeolite shows a step in the uptake at low pressure ( $p/p_0 < 0.1$ ) which indicates that it is not efficient for heat pump applications, since high temperatures are needed for desorption ( $T_{des} > 600$  K). For this reason, we explored the efficiency of high silica FAU (HS-FAU) with Si/Al  $\approx$  100. The presence of Al atoms and Na cations results in sufficient hydrophilicity to ensure the water adsorption at operational conditions. Figure S7 shows the calculated adsorption isotherm of water in HS-FAU at 298 K and Figure S6 the comparison of experimental data measured in this work and the calculated adsorption isobar at 2000 Pa.

We found that the selection of the regeneration conditions of the working pair is crucial for the effective performance. Here, we established a working pressure based on the pressure of the step in the adsorption isotherm. The value of this pressure is the one that shows an uptake near to saturation but with a low value of  $p/p_0$ . Figure S8 shows the adsorption isobars of water in HS-FAU at 700 Pa, 900 Pa, 1200 Pa, and 1700 Pa (0.22-0.53  $p/p_0$ ) which shows that variations in the conditions for the regeneration process conduct to large changes in the regeneration temperature ( $T_{des}$ ). Specifically for HS-FAU the  $T_{des}$  needed for the system increase with the pressure (20 °C in the selected pressures). The pressure control is a mechanism to improve the efficiency of the system due to it can decrease the regeneration temperature. Using the described criterion, we calculated adsorption isobars of water in HS-FAU, MOF-841, and ZJNU-30 at 700 Pa, 800 Pa and 1000 Pa, respectively, corresponding to approximately 22, 25 and 30 % RH at room temperature. Figure 5 shows that at these conditions the regeneration is achieved with a 20-23 °C temperature lift for MOF-841 and ZJNU-30 and 40 °C for HY-FAU (283 to 323 K). The first temperature lift is the range required for an air conditioner applications.<sup>76</sup> MOF-841 is already proposed for cooling applications and for AWGs being one of the best materials with a capacity about 42 wt % of water. Rieth et al.<sup>76</sup> recently proposed a suitable alternative, CoCl(BTDD) which capacity is about 82 wt % of water. This makes this MOF one of the best candidates to generate water in realistic desert conditions. We predicted sorption capacity of about 33 wt % of water for HS-FAU, the same as for NaX but with a clear improvement in the regeneration process. This makes HS-FAU better candidate than NaX for AHP and AWGs applications. ZJNU-30 shows high stability, and no alteration is exhibited in the surface area with the exposition to the air for one month, and it losses only a 14 % of surface area after one week in liquid water.<sup>43</sup> Based on the characteristic curve (Figure 6a), at realistic conditions, 318 K and 5 % RH (day) and 298 K and 35 % RH (night), we calculated the deliverable capacity of water

(Figure 6b). We reproduced water capacity of MOF-841 and we predict that ZJNU-30 captures 100.5 wt % water, taking into account the surface area losses. This Zr-based MOF shows the highest capacity reported until now and becomes the best candidate for water generation propose. The improvement in the regeneration process of HS-FAU comparing with NaX is also reflected in the release of water in day-night cycles under realistic conditions. HS-FAU shows 32 wt % of water while NaX is not an efficient candidate with only 10 wt % water.

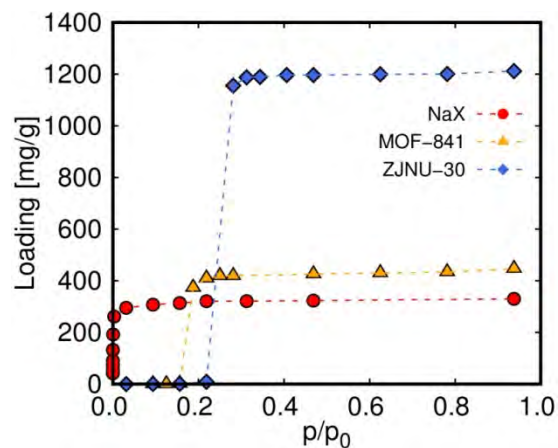
Figure 7a shows the working volume as a function of the regeneration temperature. The lowest  $T_{des}$  at which the water capacity reaches a maximum value is 303 K for ZJNU-30 at 1000 Pa, 313 K for MOF-841 at 800 Pa, and 323 K for HS-FAU at 700 Pa. Figure 7b shows the volumetric heat energy released to the condenser ( $Q_{con}$ ) as a function of temperature lift ( $T_{des}-T_{ev}$ ) where  $T_{ev}$  is fixed at 283 K and  $T_{des}$  goes from 298 K to 343 K. The highest  $Q_{con}$ , the highest cooling capacity is obtained. From this, we obtained the temperature lift which achieves a maximum cooling capacity. The ideal regeneration temperature should guarantee the maximum energy transferred and also maintain the highest working volume. In this case, the chosen  $T_{des}$  is 303 K for ZJNU-30 which corresponds to temperature lift of 20 K, 313 K (temperature lift of 30 K) for MOF-841, and 323 K (temperature lift of 40 K) for HS-FAU. The working pair ZJNU-30-water exhibits a great performance of heat transfer. The energy released with a temperature lift of 20 K is 550 kWh/m<sup>3</sup>. It is the highest cooling capacity per cycle obtained considering the regeneration temperature.<sup>11, 76</sup> The energy released to the condenser is directly related to the coefficient of performance. The coefficient of performance (COP) is the most commonly used parameter to describe the energetic efficiency of a heat pump.<sup>8, 13</sup> For cooling devices the COP is defined as the ratio of useful cold energy output divided by input heat energy,  $COP = Q_{ev}/Q_{reg}$ , more details can be found in the Supporting Information. We estimated the COP for HS-FAU, MOF-841, and ZJNU-30 using  $T_{ev}=283$  K,  $T_{con}=298$  K, and  $T_{des}=323, 313, 303$  K, respectively. At these conditions HS-FAU has a COP=0.42, MOF-841 has a COP=0.7, and ZJNU-30 shows a COP=0.948 of efficiency for cooling applications, being the highest reported COP up to date.<sup>11, 76</sup>

Figure 8 shows the heat of adsorption of the studied structures at low coverage and near saturation conditions. Low coverage corresponds to the loading at  $T_{des}$  in each structure and high loading at  $T_{ev}=283$  K (see Figure 5). The preferential sites of adsorption for FAU topology zeolites are near the Al atoms and cations which provide the hydrophilic character to the structure. Once the preferential sites are occupied, water molecules are forced to be adsorbed at less favorable sites. Two different type of behavior can be observed: NaX shows high interactions with the structure in addition to the adsorbate-adsorbate energy contribution due to water nucleation. For HS-FAU, once the more favorable adsorption sites are occupied, the interaction of the structure decreases. Therefore the heat of adsorption decreases. In this case the adsorption is due to water-water interaction and nucleation. Their hydrophilic nature is also responsible of the low difference between the heat of adsorption at saturation and low loading conditions. MOF-841 and ZJNU-30 are more hydrophobic materials and the interaction with the structure is lower than for the studied zeolites. As in the case of HS-FAU, adsorption is induced by confinement in the pores (water-walls interactions) and the step in the adsorption is due to the water-water interaction and their nucleation within the cavities of the structure. Their hydrophobic nature makes possible the largest differences between the heat of adsorption at saturation and low loading.

Besides the thermodynamic properties, the dynamic properties of the system are crucial for AHP and DCS applications which has implications for the power of charging and discharging. We performed Molecular Dynamics simulations to study the transport of water within the pores of the structures under study at saturation conditions. Figure 9 shows the Arrhenius plot of the working pairs using the self-diffusion coefficient as a function of the inverse of the temperature. The slope of the fitting line is proportional to the activation energy ( $E_A$ ) (eq 3). At fixed temperature, the hierarchy of the self-diffusion coefficients of water is ZJNU-30 > HS-FAU > MOF-841 > NaX (Figure S10). The activation energy follows the trend NaX > MOF-841 > ZJNU-30 > HS-FAU. The  $E_A$  of water in HY-FAU is similar to that of water in the bulk phase (about 18 kJ/mol) which implies the absence of diffusion limitations. There are also slight differences between the activation energy of water in ZJNU-30 and MOF-841 and water in the bulk phase, 2.5 and 3.1 kJ/mol respectively. The highest value is obtained for NaX due to the strongest interaction of water with the cations of the zeolite. The self-diffusion coefficient is usually proportional to the pore size. However, the self-diffusion coefficient for NaX is lower than for HS-FAU, although they have similar pore size, due to the more hydrophilic nature of NaX.

## CONCLUSIONS

We showed that the composition of the structure strongly affects the water adsorption in FAU-topology zeolites. The Al atom content and the proper selection of the pressure for the regeneration process reveal that high silica faujasite (HS-FAU) is a suitable candidate for water capture and release. This material also shows high self-diffusion coefficients at saturation conditions and low  $E_A$ . We found that a combination of properties of ZJNU-30 make this material a promising candidate for cooling applications and atmospheric water generator. In this case, the adsorption mechanism makes the difference. The step in adsorption takes place at  $p/p_0=0.22$  due to the combination of the cage sizes. Water adsorption starts in the small cages, then adsorbed molecules cross to intermediate cages and the big cages by nucleation and diffusion. This is responsible for the high sorption capacity of the structure. It is remarkable that ZJNU-30 exhibits records in water capacity (1200 mg/g), cooling capacity (550 kWh/m<sup>3</sup>), and COP for cooling applications (0.948). Due to the size of the cages, the diffusion of water within the pores is the highest of the studied structures. The procedure used in this work may be useful to explore new materials and the optimal conditions for AHP and AWGs applications. Based on our findings, we propose the search of structures with interconnected cages of different sizes; small enough to ensure the water adsorption at relatively low pressures (near to  $p/p_0=0.3$ ) and other cages should be near to critical diameter, to ensure a high water capacity.



**Figure 3.** Calculated adsorption isotherms of water in NaX (red), MOF-841 (yellow), and ZJNU-30 (blue) at 298 K.

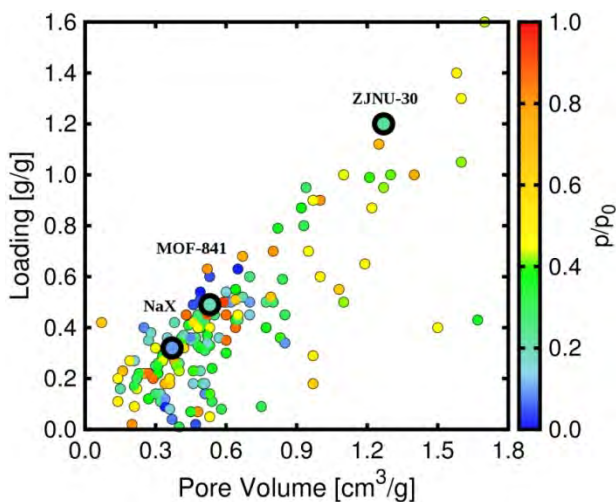


**Figure 4.** Comparison of the water capacity as a function of the pore volume in several structures. The values are taken from literature<sup>11</sup> and from this work at saturation conditions. The color map indicates the relative pressure at which the step takes place.

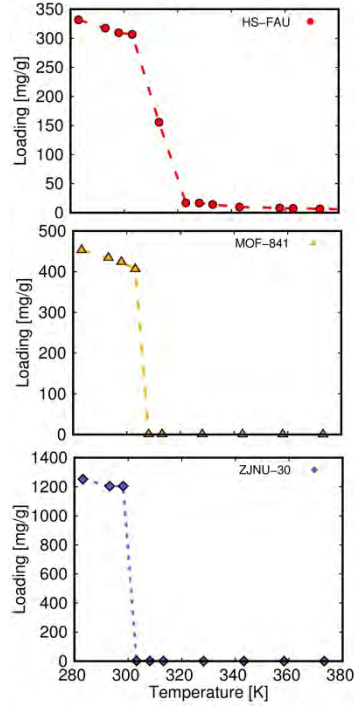


**Figure 5.** Calculated adsorption isobars from MC simulations of water in (a) HS-FAU (Si/Al=100) at 700 Pa, (b) MOF-841 at 800 Pa, and (c) ZJNU-30 at 1000 Pa.

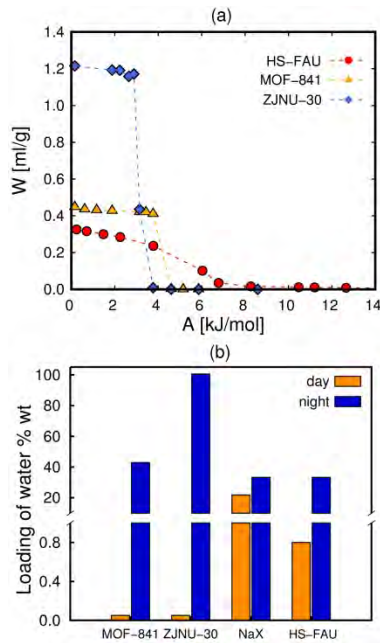


**Figure 6.** (a) Characteristic curves of HS-FAU, MOF-841, and ZJNU-30 determined using Eqs 1 and 2 and (b) water capacity at realistic desert conditions (day 318 K and 5% RH, night 298 K and 35% RH).

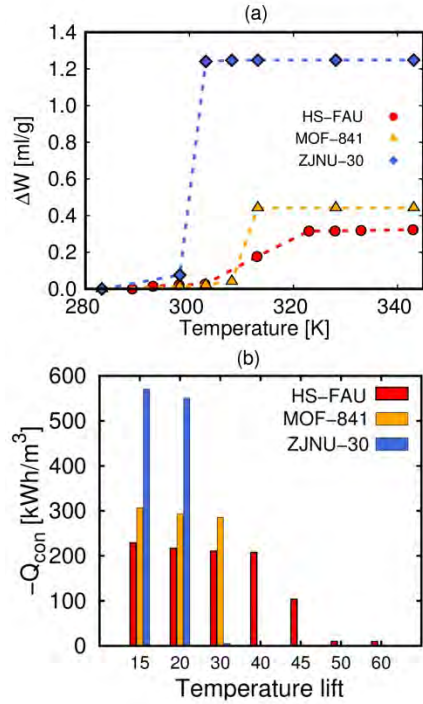


**Figure 7.** (a) Working volume as a function of the regeneration temperature ( $T_{des}$ ) at 700 Pa, 800 Pa, and 1000 Pa in HS-FAU, MOF-841, and ZJNU-30, respectively. (b) Volumetric heat energy transferred to the condenser as a function of temperature lift.

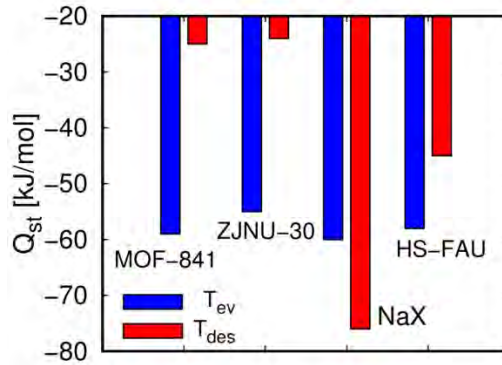


**Figure 8.** (a) Heat of adsorption for low coverage ( $T_{des}$ ) and high loading ( $T_{ev}$ )

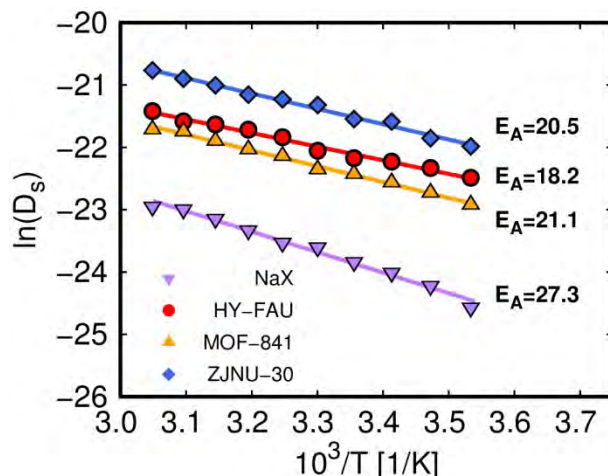


**Figure 9.** Arrhenius plot for the working pairs at saturation conditions. Lines correspond to a linear fit. The activation energies ( $E_A$ ) in kJ/mol are calculated from these slopes.

## ACKNOWLEDGEMENTS

This work was supported by the Spanish Ministerio de Economía y Competitividad (CTQ2016-80206-P). We thank C3UPO for the HPC support. Andrzej Sławek obtained financial resources as part of financing the doctoral scholarship from the National Science Center, Poland Grant No. 2018/28/T/ST5/00274.

## REFERENCES

1. M. Isaac and D. P. Van Vuuren, *Energy Policy*, 2009, **37**, 507-521.
2. S. K. Henninger, H. A. Habib and C. Janiak, *J. Am. Chem. Soc.*, 2009, **131**, 2776-2777.
3. N. Srivastava and I. Eames, *Appl. Therm. Eng.*, 1998, **18**, 707-714.
4. R. Critoph, *Int. J. Refrig.*, 2012, **3**, 490-493.
5. M. Kanamori, M. Hiramatsu, K. Katsurayama, F. Watanabe, H. Matsuda and M. Hasatani, *J. Chem. Eng. Jpn.*, 1997, **30**, 434-439.
6. H. Demir, M. Mobedi and S. Ülkü, *Renewable Sustainable Energy Rev.*, 2008, **12**, 2381-2403.
7. B. Saha, I. El-Sharkawy, A. Chakraborty and S. Koyama, *Int. J. Refrig.*, 2007, **30**, 86-95.
8. F. Jeremias, V. Lozan, S. K. Henninger and C. Janiak, *Dalton Trans.*, 2013, **42**, 15967-15973.
9. Y. I. Aristov, *Appl. Therm. Eng.*, 2013, **50**, 1610-1618.
10. F. Jeremias, A. Khutia, S. K. Henninger and C. Janiak, *J. Mater. Chem.*, 2012, **22**, 10148-10151.
11. M. F. de Lange, K. J. Verouden, T. J. Vlugt, J. Gascon and F. Kapteijn, *Chem. Rev.*, 2015, **115**, 12205-12250.
12. R. Critoph and Y. Zhong, *Proc. Inst. Mech. Eng., Part E*, 2005, **219**, 285-300.
13. M. Pons, F. Meunier, G. Cacciola, R. Critoph, M. Groll, L. Puigjaner, B. Spinner and F. Ziegler, *Int. J. Refrig.*, 1999, **22**, 5-17.
14. M. A. Lambert and B. J. Jones, *J. Thermophys. Heat Transfer*, 2005, **19**, 471-485.
15. A. Demessence, P. Horcajada, C. Serre, C. Boissière, D. Grosso, C. Sanchez and G. Férey, *Chem. Commun.*, 2009, 7149-7151.
16. T. J. Barton, L. M. Bull, W. G. Klemperer, D. A. Loy, B. McEnaney, M. Misono, P. A. Monson, G. Pez, G. W. Scherer and J. C. Vartuli, *Chem. Mater.*, 1999, **11**, 2633-2656.

17. J. M. Castillo, J. Silvestre-Albero, F. Rodriguez-Reinoso, T. J. H. Vlught and S. Calero, *Phys. Chem. Chem. Phys.*, 2013, **15**, 17374-17382.
18. S. Kitagawa, R. Kitaura and S. Noro, *Angew. Chem., Int. Ed.*, 2004, **43**, 2334-2375.
19. D. J. Tranchemontagne, J. L. Mendoza-Cortés, M. O'Keeffe and O. M. Yaghi, *Chem. Soc. Rev.*, 2009, **38**, 1257-1283.
20. J. van den Bergh, C. Gücüyener, E. A. Pidko, E. J. Hensen, J. Gascon and F. Kapteijn, *Chem. - Eur. J.*, 2011, **17**, 8832-8840.
21. J.-R. Li, R. J. Kuppler and H.-C. Zhou, *Chem. Soc. Rev.*, 2009, **38**, 1477-1504.
22. L. J. Murray, M. Dincă and J. R. Long, *Chem. Soc. Rev.*, 2009, **38**, 1294-1314.
23. H. J. Choi, M. Dincă, A. Dailly and J. R. Long, *Energy Environ. Sci.*, 2010, **3**, 117-123.
24. J. Lee, O. K. Farha, J. Roberts, K. A. Scheidt, S. T. Nguyen and J. T. Hupp, *Chem. Soc. Rev.*, 2009, **38**, 1450-1459.
25. H. Furukawa, F. Gándara, Y.-B. Zhang, J. Jiang, W. L. Queen, M. R. Hudson and O. M. Yaghi, *J. Am. Chem. Soc.*, 2014, **136**, 4369-4381.
26. J. Canivet, A. Fateeva, Y. Guo, B. Coasne and D. Farrusseng, *Chem. Soc. Rev.*, 2014, **43**, 5594-5617.
27. N. C. Burtch, H. Jasuja and K. S. Walton, *Chem. Rev.*, 2014, **114**, 10575-10612.
28. C. Wang, X. Liu, N. K. Demir, J. P. Chen and K. Li, *Chem. Soc. Rev.*, 2016, **45**, 5107-5134.
29. D.-X. Xue, Y. Belmabkhout, O. Shekhah, H. Jiang, K. Adil, A. J. Cairns and M. Eddaoudi, *J. Am. Chem. Soc.*, 2015, **137**, 5034-5040.
30. H. Kim, S. Yang, S. R. Rao, S. Narayanan, E. A. Kapustin, H. Furukawa, A. S. Umans, O. M. Yaghi and E. N. Wang, *Science*, 2017, **356**, 430-434.
31. P. Deria, D. A. Gómez-Gualdrón, W. Bury, H. T. Schaefer, T. C. Wang, P. K. Thallapally, A. A. Sarjeant, R. Q. Snurr, J. T. Hupp and O. K. Farha, *J. Am. Chem. Soc.*, 2015, **137**, 13183-13190.
32. O. V. Gutov, W. Bury, D. A. Gomez-Gualdrón, V. Krungleviciute, D. Fairen-Jimenez, J. E. Mondloch, A. A. Sarjeant, S. S. Al-Juaid, R. Q. Snurr and J. T. Hupp, *Chem. - Eur. J.*, 2014, **20**, 12389-12393.
33. J. E. Mondloch, M. J. Katz, N. Planas, D. Semrouni, L. Gagliardi, J. T. Hupp and O. K. Farha, *Chem. Commun.*, 2014, **50**, 8944-8946.
34. J. Canivet, J. Bonnefoy, C. Daniel, A. Legrand, B. Coasne and D. Farrusseng, *New J. Chem.*, 2014, **38**, 3102-3111.
35. B. Coasne, K. E. Gubbins and R. J.-M. Pellenq, *Adsorption*, 2005, **11**, 289-294.
36. B. Coasne, A. Galarneau, R. J. Pellenq and F. Di Renzo, *Chem. Soc. Rev.*, 2013, **42**, 4141-4171.
37. W. J. Sarni and D. S. Grant, in *Water Stewardship and Business Value*, ROUTLEDGE in association with GSE Research, 2018, vol. 97, pp. 97-138.
38. UNHR, The human right to water and sanitation (A/RES/64/292), [http://ap.ohchr.org/documents/dpage\\_e.aspx?m=167](http://ap.ohchr.org/documents/dpage_e.aspx?m=167), Accessed 07/13/2018.
39. L. Cáceres, B. Gómez-Silva, X. Garró, V. Rodríguez, V. Monardes and C. P. McKay, *J. Geophys. Res.: Biogeosci.*, 2007, **112**.
40. H. E. Unland, P. R. Houser, W. J. Shuttleworth and Z.-L. Yang, *Agric. For. Meteorol.*, 1996, **82**, 119-153.
41. M. A. Shannon, P. W. Bohn, M. Elimelech, J. G. Georgiadis, B. J. Marinas and A. M. Mayes, in *Nanoscience And Technology: A Collection of Reviews from Nature Journals*, World Scientific, 2010, pp. 337-346.
42. M. Elimelech and W. A. Phillip, *Science*, 2011, **333**, 712-717.
43. H. M. Liu, Y. B. He, J. J. Jiao, D. J. Bai, L. Chen, R. Krishna and B. L. Chen, *Chem. - Eur. J.*, 2016, **22**, 14988-14997.
44. B. Huang, A. McGaughey and M. Kaviany, *Int. J. Heat Mass Transfer*, 2007, **50**, 393-404.

45. B. Huang, Z. Ni, A. Millward, A. McGaughey, C. Uher, M. Kaviani and O. Yaghi, *Int. J. Heat Mass Transfer*, 2007, **50**, 405-411.
46. D. Liu, J. Purewal, J. Yang, A. Sudik, S. Maurer, U. Mueller, J. Ni and D. Siegel, *Int. J. Hydrogen Energy*, 2012, **37**, 6109-6117.
47. Y. Ming, H. Chi, R. Blaser, C. Xu, J. Yang, M. Veenstra, M. Gaab, U. Müller, C. Uher and D. J. Siegel, *Int. J. Heat Mass Transfer*, 2015, **82**, 250-258.
48. H. W. B. Teo, A. Chakraborty, Y. Kitagawa and S. Kayal, *Int. J. Heat Mass Transfer*, 2017, **114**, 621-627.
49. D. Frenkel and B. Smit, *Understanding molecular simulation: from algorithms to applications*, 2002.
50. P. Mark and L. Nilsson, *J. Phys. Chem. A*, 2001, **105**, 9954-9960.
51. S. L. Mayo, B. D. Olafson and W. A. Goddard, *J. Phys. Chem*, 1990, **94**, 8897-8909.
52. A. K. Rappe, C. J. Casewit, K. S. Colwell, W. A. Goddard and W. M. Skiff, *J. Am. Chem. Soc.*, 1992, **114**, 10024-10035.
53. C. Lehmann, S. Beckert, R. Gläser, O. Kolditz and T. Nagel, *Appl. Energy*, 2017, **185**, 1965-1970.
54. J. Baker, *J. Comput. Chem.*, 1986, **7**, 385-395.
55. M. Sanders, M. Leslie and C. Catlow, *J. Chem. Soc., Chem. Commun.*, 1984, 1271-1273.
56. R. Jackson and C. Catlow, *Mol. Simul.*, 1988, **1**, 207-224.
57. D. Dubbeldam, S. Calero, D. E. Ellis and R. Q. Snurr, *Mol. Simul.*, 2015, **42**, 81-101.
58. D. Dubbeldam, A. Torres-Knoop and K. S. Walton, *Mol. Simul.*, 2013, **39**, 1253-1292.
59. D. Dubbeldam and R. Q. Snurr, *Mol. Simul.*, 2007, **33**, 305-325.
60. C. E. Wilmer, K. C. Kim and R. Q. Snurr, *J. Phys. Chem. Lett.*, 2012, **3**, 2506-2511.
61. M. Dubinin, *Bull. Acad. Sci. USSR, Div. Chem. Sci. (Engl. Transl.)*, 1991, **40**, 1-19.
62. M. Dubinin, *Russ. Chem. Bull.*, 1960, **9**, 1072-1078.
63. S. Pronk, S. Páll, R. Schulz, P. Larsson, P. Bjelkmar, R. Apostolov, M. R. Shirts, J. C. Smith, P. M. Kasson and D. Van Der Spoel, *Bioinformatics*, 2013, **29**, 845-854.
64. B. Hess, C. Kutzner, D. Van Der Spoel and E. Lindahl, *J. Chem. Theory Comput.*, 2008, **4**, 435-447.
65. D. Van Der Spoel, E. Lindahl, B. Hess, G. Groenhof, A. E. Mark and H. J. Berendsen, *J. Comput. Chem.*, 2005, **26**, 1701-1718.
66. H. J. Berendsen, D. van der Spoel and R. van Drunen, *Comput. Phys. Commun.*, 1995, **91**, 43-56.
67. S. Nosé, *Mol. Phys.*, 1984, **52**, 255-268.
68. W. G. Hoover, *Phys. Rev. A*, 1985, **31**, 1695.
69. W. Makowski, *Thermochim. Acta*, 2007, **454**, 26-32.
70. W. Makowski and Ł. Ogorzałek, *Thermochim. Acta*, 2007, **465**, 30-39.
71. J. Datka and B. Gil, *J. Catal.*, 1994, **145**, 372-376.
72. A. Slawek, J. M. Vicent-Luna, B. Marszałek, S. R. G. Balestra, W. Makowski and S. Calero, *J. Phys. Chem. C*, 2016, **120**, 25338-25350.
73. A. Sławek, J. M. Vicent-Luna, B. Marszałek, W. Makowski and S. Calero, *J. Phys. Chem. C*, 2017, **121**, 25292-25302.
74. G. Akiyama, R. Matsuda, H. Sato, A. Hori, M. Takata and S. Kitagawa, *Microporous Mesoporous Mater.*, 2012, **157**, 89-93.
75. A. Khutia, H. U. Rammelberg, T. Schmidt, S. Henninger and C. Janiak, *Chem. Mater.*, 2013, **25**, 790-798.
76. A. J. Rieth, S. Yang, E. N. Wang and M. Dincă, *ACS Cent. Sci.*, 2017, **3**, 668-672.



# Enhancing the Water Capacity in Zr-based Metal Organic Framework for Heat Pump and Atmospheric Water Generator Applications

A. Luna-Triguero<sup>a</sup>, A. Sławek<sup>b</sup>, H. P. Huinink<sup>c</sup>, T. J. H. Vlugt<sup>d</sup>, A. Poursaeidesfahani<sup>d</sup>, J.M. Vicent-Luna<sup>a\*</sup>, and S. Calero<sup>a,c\*</sup>

<sup>a</sup>Department of Physical, Chemical and Natural Systems, Universidad Pablo de Olavide, Ctra. Utrera Km. 1, Seville ES-41013, Spain

<sup>b</sup> Faculty of Chemistry, Jagiellonian University, Gronostajowa 2, 30-387 Kraków, Poland

<sup>c</sup> Department of Applied Physics, Eindhoven University of Technology, P.O. Box 513, 5600 MB Eindhoven, The Netherlands. <sup>d</sup> Engineering Thermodynamics, Process & Energy Department, Faculty of Mechanical, Maritime and Materials Engineering, Delft University of Technology, Leeghwaterstraat 39, 2628CB Delft, The Netherlands

Corresponding authors:

Email: [jmviiclun@upo.es](mailto:jmviiclun@upo.es)

Email: [scalero@upo.es](mailto:scalero@upo.es)

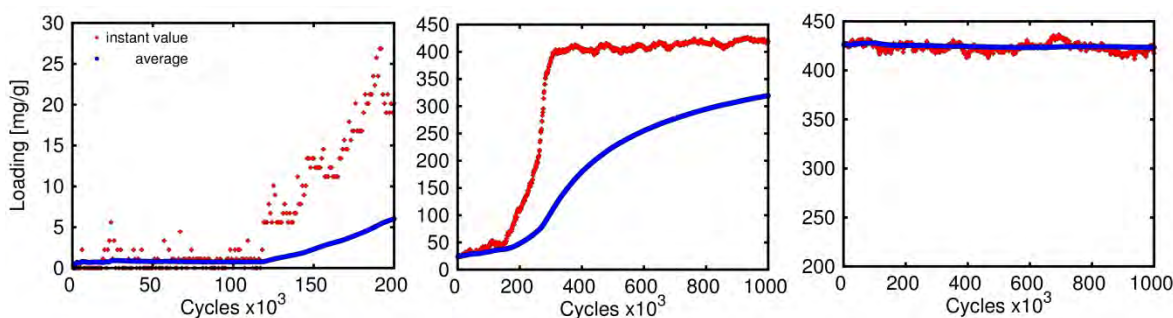


**Figure S1.** Equilibration of water adsorption in MOF-841 at 800 Pa and 298 K as a function of the number of production runs. Instant values of adsorption in red and average in blue.

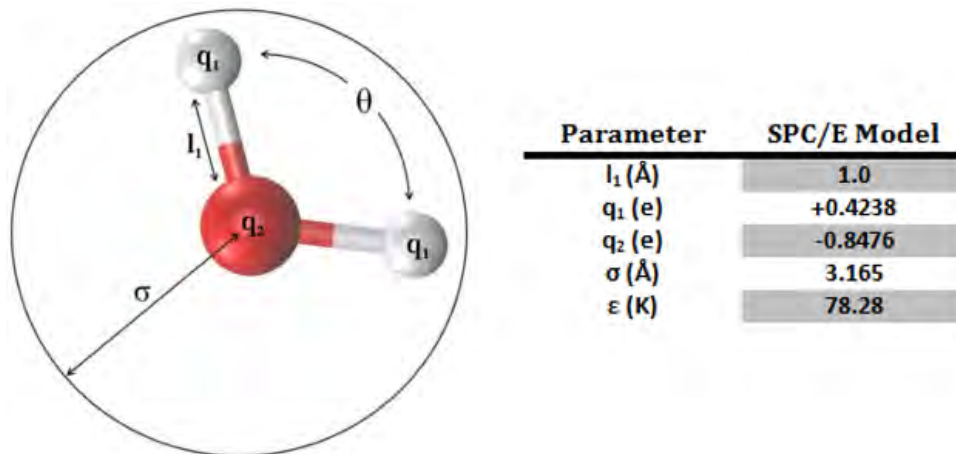


**Figure S2.** SPC/E water model with geometrical and force-field parameters.<sup>1</sup>

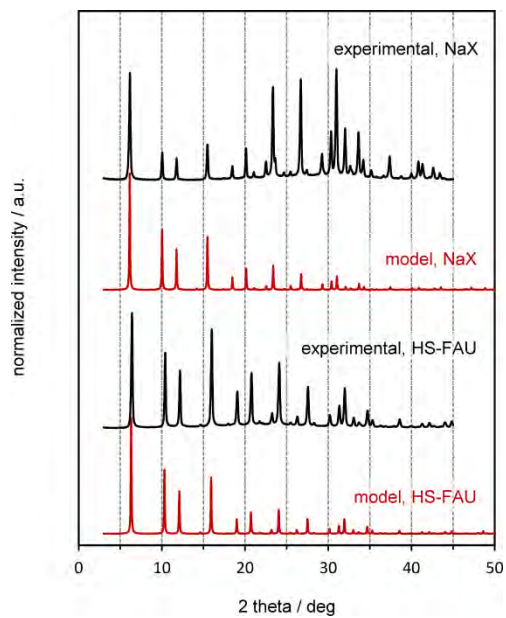


**Figure S3.** Comparison of the experimental and modeled XRD patterns of the studied Faujasites. For clarification, intensities of all peaks except the one at ca 6° of the modeled patterns were multiplied by a factor 3.

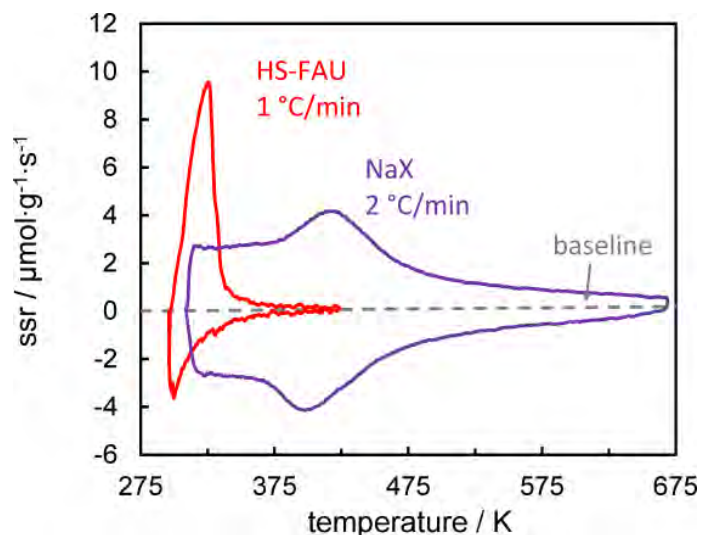


**Figure S4.** QE-TPDA profiles for water in HS-FAU ( $\text{Si/Al} > 100$ ) and NaX ( $\text{Si/Al} \approx 1.06$ ).  $\text{ssr}$  denotes the specific sorption rate unit, which is positive for desorption, negative for adsorption, and equal to zero when the initial concentration of the adsorbate is not changed. Values of partial pressures of water steam were equal to 2000 Pa for HS-FAU and 3100 Pa for NaX. The profiles for HS-FAU and NaX were recorded using a heating/cooling rate of 1 and 2 °C/min, respectively.

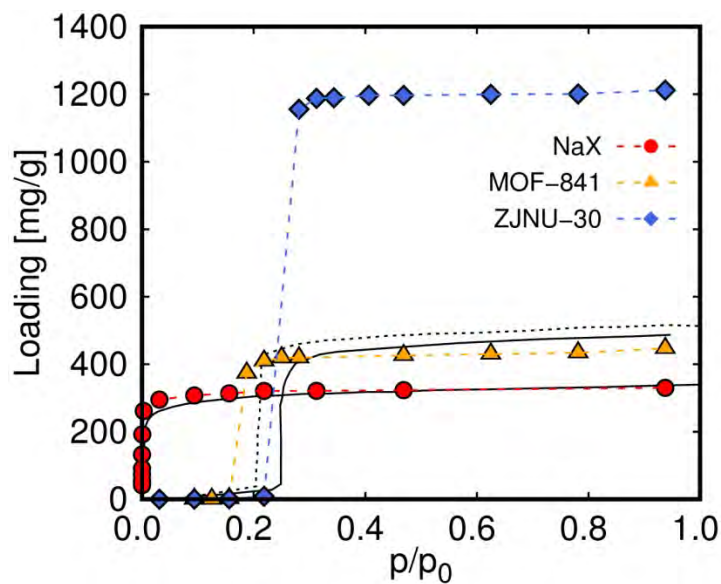


**Figure S5.** Comparison of computed adsorption isotherms of water in NaX (red) and MOF-841 (yellow) at 298 K. Experiments (black lines) are taken from literature.<sup>2,3</sup>

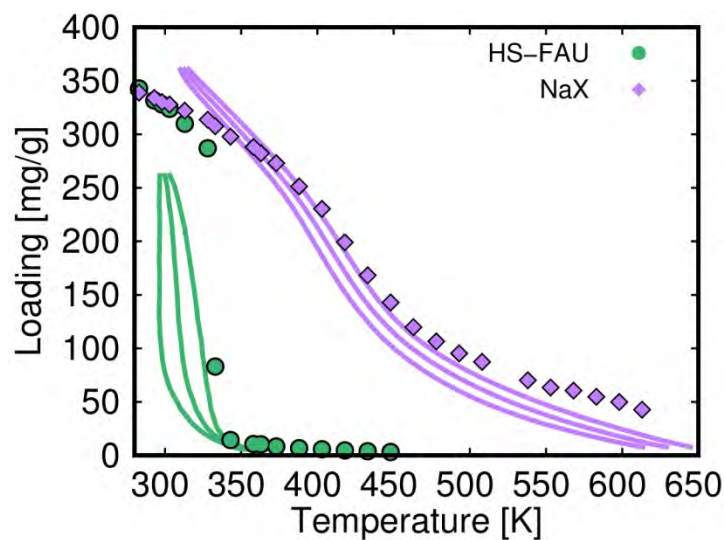


**Figure S6.** Comparison of adsorption isobars of water in NaX (purple) at 3100 Pa and HS-FAU (green) at 2000 Pa. Simulations (symbols) and experiments measured in this work (lines). For each experiment three curves are plotted. The one shifted to higher temperatures stands for desorption, while the one shifted to lower temperatures for adsorption. Averaging of adsorption and desorption curves leads to obtaining actual adsorption isobar reflected the intermediate curve.

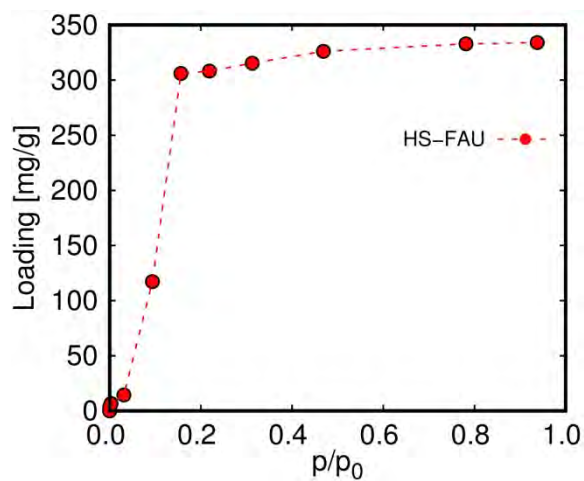


**Figure S7.** Calculated adsorption isotherm of water in HS-FAU at 298 K.  $p_0$  is the vapor pressure of water at room temperature (3100 Pa)

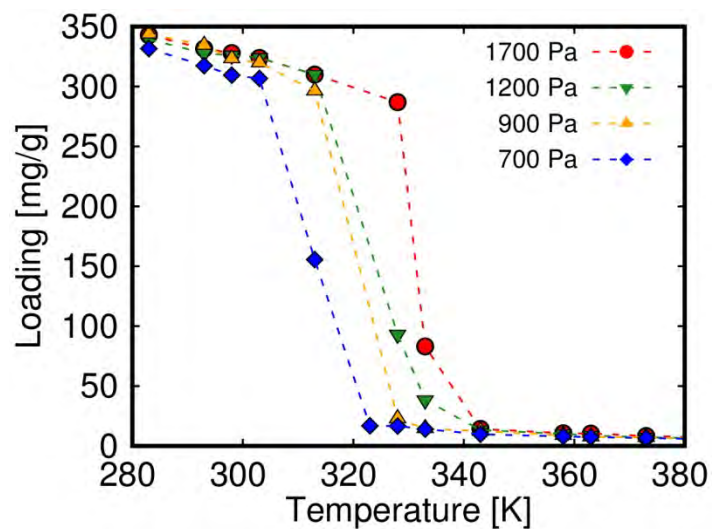


**Figure S8.** Calculated adsorption isobars of water in HS-FAU at 700, 900, 1200, and 1700 Pa.

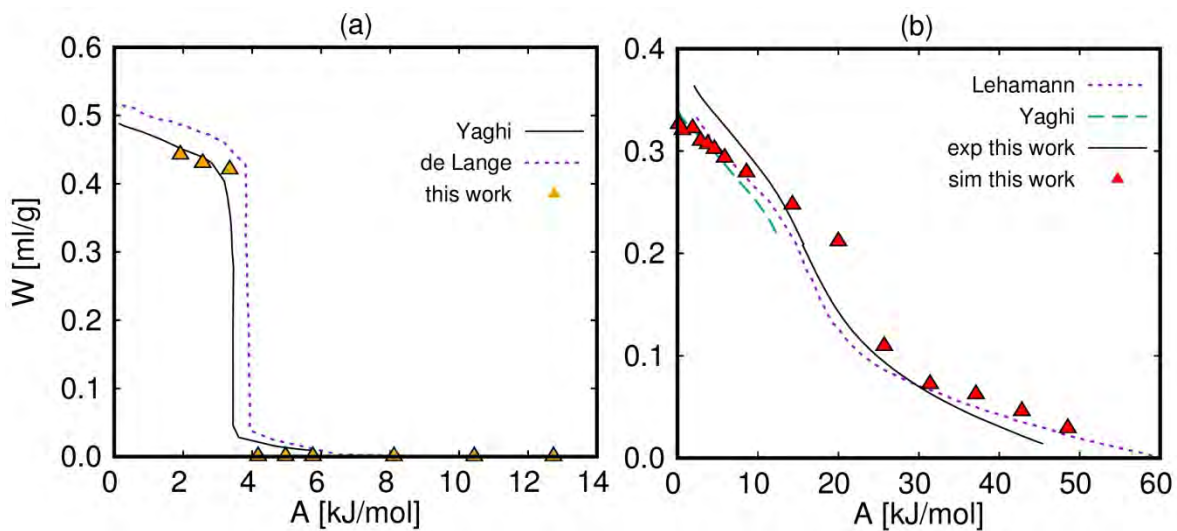


**Figure S9.** Comparison of calculated characteristic curves from simulations (symbols) and experiments (lines) for (a) MOF-841 and (b) NaX. Experiments are taken from the literature<sup>2-4</sup> and measured in this work (NaX).

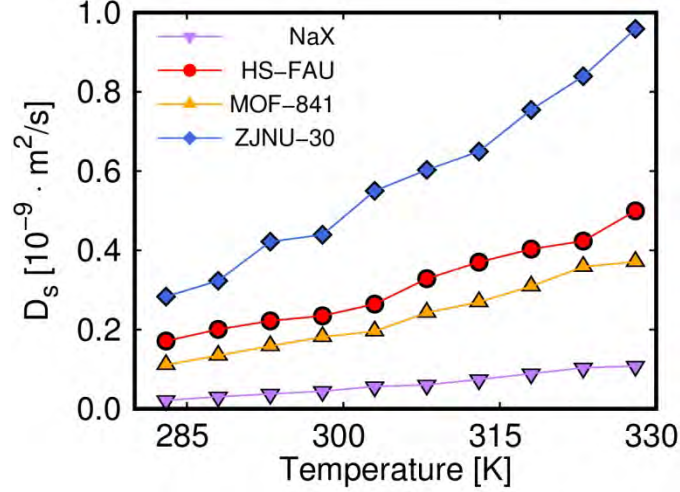


**Figure S10.** Diffusion coefficient of water in ZJNU-30 (blue), MOF-841(yellow), HS-FAU (red), and NaX (purple) as a function of temperature at calculated saturation.

### Thermodynamic model

We used the thermodynamic model described by de Lange et al. <sup>3</sup> to calculate the energies and the coefficient of performance (COP) of the systems. The steps of the process are as depicted in the diagram of the isosteric cycle of an AHP (Figure 1b).

Energy of the evaporator:

$$Q_{ev} = \frac{-\Delta H_{vap}(T_{ev})\rho_{liq}m_s\Delta W}{M_w}$$

Energy of the condenser:

$$Q_{con} = \frac{\Delta H_{vap}(T_{con})\rho_{liq}m_s\Delta W}{M_w}$$

Energy needed in the regeneration:

$$Q_{reg} = Q_{1-2} + Q_{2-3}$$

$$Q_{1-2} = \int_{T_{con}}^{T_2} c_p^{ef}(T)dT + \int_{T_{con}}^{T_2} \rho_{liq}W_{max}c_p^w(T) dT$$

$$Q_{2-3} = \int_{T_2}^{T_{des}} c_p^{ef}(T)dT + \int_{T_2}^{T_{des}} \rho_{liq} \frac{W_{max} + W_{min}}{2} c_p^w(T)dT - Q_{sorp}$$

Energy obtained in the adsorption:

$$Q_{ads} = Q_{3-4} + Q_{4-1}$$

$$Q_{3-4} = \int_{T_{des}}^{T_3} c_p^{ef}(T) dT + \int_{T_{des}}^{T_3} \rho_{liq} W_{max} c_p^w(T) dT$$

$$Q_{4-1} = \int_{T_3}^{T_{con}} c_p^{ef}(T) dT + \int_{T_3}^{T_{con}} \rho_{liq} \frac{W_{max} + W_{min}}{2} c_p^w(T) dT + Q_{sorp}$$

Energy released in the adsorption:

$$Q_{sorp} = \frac{1}{M_w} \int_{W_{min}}^{W_{max}} \rho_{liq} \Delta H_{ads}(W) dW$$

$\Delta H_{vap}$  is the enthalpy of evaporation,  $m_s$  is the amount of adsorbent used in adsorption,  $\Delta W$  is the working capacity,  $\rho_{liq}$  is the density,  $M_w$  is the molar mass of water,  $\Delta H_{vap}$  is the enthalpy of adsorption,  $c_p^{ef}$  is the heat capacity of water and  $c_p^w$  is the heat capacity of the material.

We assumed that (1) the heat capacity of the adsorbent is 1 J/g K and this value is independent of the temperature; (2) mass transfer limitations are neglected as studies of mass transport in MOFs are scarce and often unknown

**Table S1.** Aluminosilicate-water Lennard-Jones parameters and partial charges.

Atom	O <sub>Al</sub>		O <sub>Si</sub>		Na <sup>+</sup>	
	$\epsilon$ [K]	$\sigma$ (Å)	$\epsilon$ [K]	$\sigma$ (Å)	$\epsilon$ [K]	$\sigma$ (Å)
O <sub>w</sub>	80	3.3	80	3.3	50	3.3
Atom	O <sub>Al</sub>	O <sub>Si</sub>	Si	Al	Na <sup>+</sup>	
q [e]	-1.20	-1.025	2.05	1.75	1.0	

O<sub>AL</sub> are oxygen atoms that are bridging one Si and one Al atom, O<sub>SI</sub> are oxygen atoms that are bridging two Si atoms, and O<sub>w</sub> are the oxygen atoms of water.

1. Water models, [http://www1.lsbu.ac.uk/water/water\\_models.html](http://www1.lsbu.ac.uk/water/water_models.html), (accessed 07/13/2018).
2. H. Furukawa, F. Gándara, Y.-B. Zhang, J. Jiang, W. L. Queen, M. R. Hudson and O. M. Yaghi, *J. Am. Chem. Soc.*, 2014, **136**, 4369-4381.
3. M. F. de Lange, K. J. Verouden, T. J. Vlugt, J. Gascon and F. Kapteijn, *Chem. Rev.*, 2015, **115**, 12205-12250.
4. C. Lehmann, S. Beckert, R. Gläser, O. Kolditz and T. Nagel, *Applied Energy*, 2017, **185**, 1965-1970.